Measuring Effective Stiffness of Li-ion Batteries via Acoustic Signal Processing

SCHOLARONE™
Manuscripts

Measuring Effective Stiffness of Li-ion Batteries via Acoustic Signal Processing

Wesley Chang[1,4,6,7], Robert Mohr[6,7], Andrew Kim[3,4], Abhi Raj[3,4], Greg Davies[4], Kate Denner[1], Jeung Hun Park[1,2,4,6,*], and Daniel Steingart[1,2,4,5,6,7,*]

[1]Department of Mechanical and Aerospace Engineering, [2]Department of Chemical and Biological Engineering, [3]Department of Electrical Engineering, and [4]Andlinger Center for Energy and the Environment, Princeton University, Princeton, NJ 08540 USA,

[5]Department of Earth and Environmental Engineering, [6]Department of Chemical Engineering, and [7]Columbia Electrochemical Energy Center, Columbia University, New York, NY 10027 USA

*Correspondence: dan.steingart@columbia.edu (D.S.), jeungp@princeton.edu (J.H.P.)

ABSTRACT

In this work we build upon acoustic-electrochemical correlations to investigate the relationships between sound wave structure and chemo-mechanical properties of a pouch cell battery. Cell thickness imaging and wave detection during pouch cell cycling are conducted in parallel. Improved acoustic hardware and signal processing are used to validate the direct measurement of material stiffness, which is an intrinsic physical property. Measurement of cell thickness to micron resolution and wave transmit time to nanosecond resolution in a temperature and pressure controlled acoustic rig allows for estimation of the effective stiffness. We further explore the effects of material type and cell layering on the acoustic signal, demonstrating that the *operando* acoustic method can accurately measure the changes in physical state properties of a battery with high dynamic temporal and spatial range.

KEYWORDS: acoustic ultrasound, operando, transmission X-ray microscopy, Li-ion battery, stiffness, elastic modulus

1

1. INTRODUCTION

Acoustic interrogation at frequencies commensurate with physical scale is an established technique for characterizing structural materials found in geophysics[1-4], food manufacturing[5], and medical applications.[6] Recently, the acoustic interrogation technique has been adapted for use in *operando* battery state-of-charge and state-of-health analyses. Thus far, battery acoustic analysis has relied on an empirical approach of collecting experimental results under a wide range of conditions and fingerprinting the characteristic changes for pattern matching. For example, Hsieh et al.[7] correlated acoustic signals with estimated density changes simulated from continuum electrochemical modeling[8] and density values experimentally measured by Reimers and Dahn.[9] Davies et al. expanded upon this approach and used a machine learning algorithm to show that the battery state-of-charge (SOC) and state-of-health (SOH) could be predicted by the acoustic time-of-flight signal within an error of ~1%[10] while introducing a rudimentary estimate of cell stack thickness as a function of SOC/SOH. Other recent studies have demonstrated the ability of transmitted acoustic signals to effectively track cell gassing due to rapid signal attenuation in gaseous media, lithium plating on graphite during fast charge, and initial electrode wetting.[11-16] These studies rely upon the inherent link between electrochemical state and dynamic mechanical state proposed by Hsieh et al.[7], and use shifts of the overall acoustic wave to exploit this relationship. We demonstrate that acoustic signals can provide absolute measurements of an intrinsic material property such as stiffness. The true wave transmit time can be determined to measure the wave velocity, which is then used to calculate the effective stiffness of the entire cell stack.

Wave velocity can be used to measure elastic modulus, and acoustics is a common tool for understanding stiffness in composite materials. Sakamoto et al. utilized acoustic signals to measure elastic properties of solid lithium metal (7.82 GPa)[17] and $LiCoO_2$ particles (191 GPa)[18], which are comparable with Young's moduli from tensile testing. In the context of a lithium-ion cathode, $LiCoO_2$ particles and conductive carbon are mixed and cast to form a slurry composite. At this scale, the composite structure and the overall elasticity tensor become more complicated, but sound speed is a standard tool within geophysics and structural mechanics to measure complex composites.[1]

At the cell level, each of these composite electrodes is stacked together between separators and wetted by electrolyte. In this work we study the deviation of the total cell wave velocity from a simple extrapolation of the expected stack value, with hypothesized influences from the interface structure and extent of electrolyte wetting. Once these deviations are understood, the effective device stiffness can be related to electrode state.
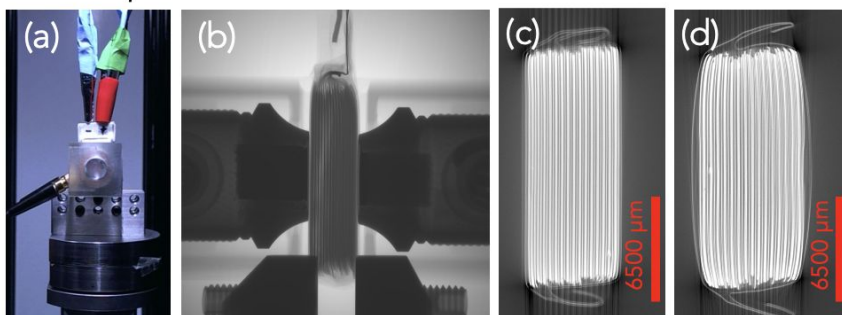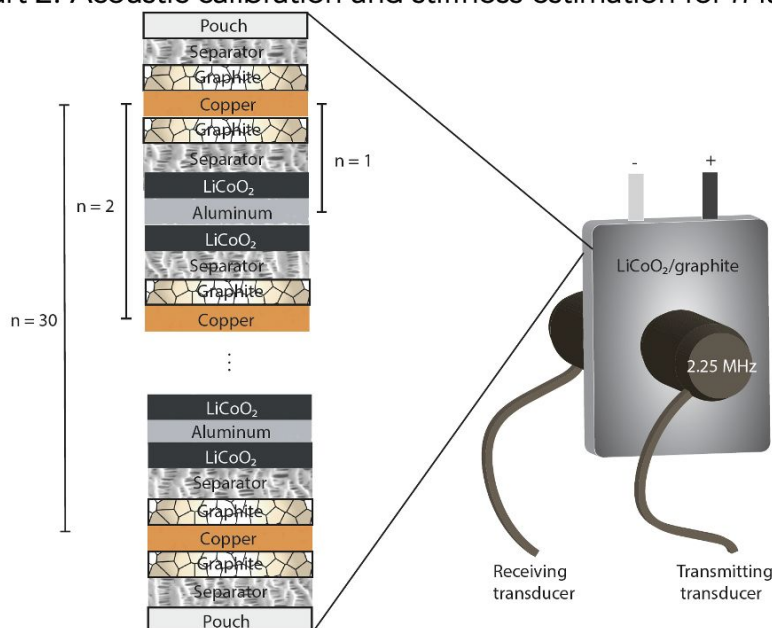
2

Part 1: *Operando* TXM/acoustics for thickness measurements

Part 2: Acoustic calibration and stiffness estimation for *n*-layered cells

Figure 1. Part 1: *Operando* TXM/acoustics for thickness imaging. (a) Optical image and (b) X-ray radiograph of 210 mAh pouch cell between the receiving and transmitting transducers, and (c) the pristine cell and (d) after mechanical expansion due to fast rate cycling. *Operando* movies of the cell at 1C, 2C and 3C cycling rates were taken. Part 2: acoustic calibration and stiffness estimation for *n*-layered cells. Schematic depicts the 30-layered commercial pouch cell, with each layer corresponding to the copper-backed graphite anode, aluminum-backed $LiCoO_2$ cathode, and separators in between the electrodes. Pouch cells of fewer layers (i.e. n = 1) were constructed with the fresh electrodes, in order to determine the effect of layering on acoustic velocity. For clarity, the electrodes were double-sided, as shown in the schematic. The results are shown in Figure 3.

2. EXPERIMENTAL

2.1 Operando thickness/acoustic characterization.
We designed an *operando* experiment with simultaneous time-resolved transmission X-ray microscopic (TXM) imaging, acoustic detection, and electrochemical cycling. TXM imaging provided high resolution real-time thickness measurements of each layer within a commercial pouch cell (see Figures 1a and 1b for depiction of setup). Figures 1c and 1d depict TXM

radiographs, with the bright, high intensity regions correlated to materials that absorb X-rays (in this case, the $LiCoO_2$ cathode and copper current collector), and the dark, low intensity regions correlated to materials that transmit X-rays (graphite anode, aluminum current collector, polypropylene/polyethylene separator, pouch bag).[19] Figure 1c depicts the TXM radiograph of a fresh cell, and Figure 1d depicts the TXM radiograph of a cell cycled at high rates, resulting in mechanical expansion. TXM imaging provides micron resolution for measurements of thickness, which is essential for calculating the wave velocity, though some of the electrode layers are not exactly perpendicular to the field of view which distorts pixel intensities. Pouch cells were mounted in a custom 3D-printed chuck (FormLabs), kept in mechanical contact with the ultrasonic transducers (Olympus, 2.25 MHz) via precision springs (Gardner) and liquid couplant gel (Sonogel), and placed in the TXM holder. X-ray radiographs were obtained *operando* with an X-radia 520 Versa (Carl Zeiss, Pleasanton, CA) using programmed Carl Zeiss software, with imaging parameters listed in Table 1. Battery cycling was performed with a Gamry Reference 3000+ potentiostat. Ultrasound measurements were performed with a commercial acoustic pulser/receiver (SIUI CTS-9009) controlled by a Linux server connected to the acoustic module via a NodeJS/ethernet interface. X-ray radiographs were taken every 20 seconds, and acoustic snapshots were taken every 5 seconds. Image drift correction was done post-imaging by shifting all images relative to a set point (the right edge of the left transducer). Images were collated into a movie (movie files M1, M2, M3 can be found in the ESI). Information on thresholds used for thickness measurements can be found in Figures S1-S5. While TXM was used in this study to produce tomographic movies of cell evolution, a simple displacement or thickness sensor could also be used. *Both cell thickness and acoustic time-of-flight measurements were obtained during cycling.*

Beam Voltage	140 kV	Source Z	100.0 mm
Objective Lens	0.4 X	Detector Z	200.0 mm
Power	10 W	Binning	2
Energy Filter	HE3	Exposure Time	20 s
Projection Angle	90°	Frames	10,000

Table 1. TXM Imaging Parameters.

2.2 Calibration and improvement of acoustic signal collection.

As acoustic interrogation is a recent technique for battery characterization, it is important that reproducibility of the acoustic signal across systems is validated. Previous published reports were focused on correlations with battery charge and health and used relative changes in the acoustic signal. However, in the present case, an absolute measurement of wave velocity requires a reproducible measurement of the signal. To confirm signal collection reliability, improvements in acoustic hardware and software were made and are described here in order to provide a useful foundation for other researchers interested in utilizing similar techniques. First, a constant pressure (1.4 ± 0.1 psi, or ~0.01 MPa) cell holder was constructed (machined out of aluminum and controlled with a linear actuator). The cell holder was placed in a temperature-controlled chamber at $30.0 \pm 0.1°C$ (Neware MWHX-200). Transducers (Olympus, 2.25 MHz) were fixed within the constant pressure holder and connected to a waveform generator and receiver (Compact Pulser and Picoscope). Unlike a commercial built-in acoustic pulser/receiver, splitting up the ultrasonic pulser/receiver ensures that the raw signal is being transmitted and read, without any internal signal smoothing/filtering. Rexolite (cross-linked polystyrene with low acoustic attenuation) spacers were used between the transducers in order to prevent near-field

(Fresnel) interference, such that the sample should only interact with the low noise far-field (Fraunhofer) acoustic waves.[20] Determination of wave arrival times was done by calibrating with a blank (e.g. Rexolite spacer, or a metal of known thickness and velocity). Cell cycling was performed with a Keithley 2401 SourceMeter. A schematic of this setup can be found in Figure S6. *Conducting pouch cell acoustic tests at constant temperature/pressure in a fixed cell holder and with a higher resolution signal generator/collector improved the overall resolution of the wave arrival time.* These results were then used to calibrate and confirm the results from the *operando* thickness/acoustic setup.

2.3. Pouch cell assembly.

Part 1: *Operando* thickness/acoustics. Commercial 210 mAh pouch cells of $LiCoO_2$/graphite chemistry in $LiPF_6$ in ethylene carbonate, dimethyl carbonate (EC:DMC, 1:1 v/v%) were used in all *operando* TXM/acoustic studies. The manufacturer specification sheet information can be found in Table S1 and cell property information in Table 2.[16] Cycling protocol used in this study can be found below in Table 3. The cells were charged to 4.5 V rather than the typical 4.2 V for $LiCoO_2$ cathodes in order to induce greater structural changes in the cell. The cells were discharged to 2.7 V. Three rates were studied (1C, 2C and 3C), with a constant current constant voltage charge protocol (with constant voltage stop current at C/30), and constant current discharge protocol at the same rate as the charge. Cycling results can be found in Figure S7.

Table 2. Cell Properties.

Electrode	# Layers	Thickness (μm)	Loading (mg/cm^2)	Density (g/cm^3)
$LiCoO_2$	30	58	8.9	1.54
Graphite	32	66	7.0	1.06

Electrode	Capacity (mAh/cm^2)	BET Surface Area (m^2/g)	BET Micropore Volume (cm^3/g)
$LiCoO_2$	2.44	2.45	0.000753
Graphite	2.60	3.18	0.000214

Table 3. Cycling Protocol.

Step	Protocol	Parameters
1	Rest	15 min
	CC Charge	Until 4.5 V
	CV Charge	At 4.5 V until C/30 or 30 min
	Rest	120 min
	CC Discharge	Until 2.7 V
	Rest	120 min
2	Rest	15 min
	CC Charge	Until 4.5 V
	CV Charge	At 4.5 V until C/30 or 30 min
	Rest	15 min
	CC Discharge	Until 2.7 V
3	Repeat step 2	4 times
4	Repeat steps 1-3	3 times

Part 2: Acoustic calibration and effective stiffness estimation.
To construct various *n*-layered pouch cells for testing the effect of cell layering on the ultrasonic velocity, fresh commercial cells were taken apart to harvest the electrodes. The same electrodes

were used to ensure consistency in measuring the wave arrival times, which are a function of material state (i.e. density and elastic modulus). A schematic of the layering configuration is shown in Figure 1. Other cell materials were purchased (aluminum and nickel tabs from MTI, 1M $LiPF_6$ in DMC and pouch bags from Sigma-Aldrich, fluoroethylene carbonate from Alfa-Aesar). The *n*-layered pouch cells were constructed in an Argon-filled glovebox (H_2O < 0.5 ppm, O_2 < 0.5 ppm), with each electrode/separator layer wetted by electrolyte and then sealed with an impulse heat sealer for 3 seconds on each side. Pouch cell thicknesses were measured in triplicate with a digital caliper, and then acoustically interrogated in the constant pressure/temperature setup (see section 2.2).

3 RESULTS AND DISCUSSION

3.1. Operando pouch cell thickness measurements with transmission x-ray microscopy
Acoustic wave velocity is determined by the speed of wave propagation through a medium with defined thickness. While the wave arrival time can be determined from the measured acoustic signal, thickness must be measured independently to verify the wave velocity. The expansion and contraction of a pouch cell during cycling can be imaged with transmission X-ray microscopy (TXM), which has sufficient range and pixel resolution to measure both the total cell thickness and the average layer thicknesses. TXM parameters were optimized with exposure time of 20 seconds, beam voltage of 140 kV, a 0.4X objective lens and 90° projection angle (Table 1). Figure 1 illustrates the experimental configuration and example radiographs of the mechanical expansion of a pouch cell upon cycling. The commercial pouch cell chosen ($LiCoO_2$/graphite, 210 mAh nominal capacity) has a total thickness of approximately 5.6 mm when fully charged. The measured thickness varies between 5.4 and 5.6 mm (~4% change) at a rate of 1C. There is less variation (~0.5%) at a rate of 3C because of less attainable capacity before hitting the 4.5 V voltage cutoff on charge. The thickness changes are dominated by the ~10% volume expansion and contraction of graphite anodes upon lithiation/delithiation[10]. With 15 double-sided anodes and cathodes, each of the 30 cell layers (one layer is defined as an anode, a cathode, with a separator layer in between each electrode) is approximately 170 μm in thickness as measured by average peak-to-peak spacing (additional information on pixel thresholds for thickness measurements can be found in Figures S1-S5).

3.2. Absolute measurement of wave velocity with improvements in acoustic hardware/software
Calibration of the acoustic signal is done by placing the transducers flush against each other to establish a zero value. The measured zero value for the transducer type used in this experiment (Olympus, 2.25 MHz) is about 0.45 μs, which is significant considering the total transmit time, as measured by the wave arrival at the receiving transducer, through the full 210 mAh pouch cell is no more than 4 μs. This non-zero value is due to the finite distance between the piezoelectric crystal within the transducer and the ceramic front plate of the transducer, the finite thickness of acoustic gel couplant applied on the surface of the transducers, as well as internal measurement inaccuracies of the portable acoustic device. The zeroed value of 0.45 μs must be subtracted from the measured wave arrival time of the 210 mAh pouch cells to determine the true transmit time. Second, the reported time was tested with several calibration metals of known thicknesses (Table 4). Given the reference sound velocities for these metals, the reported wave arrival time can be checked for accuracy. Unfortunately, the accuracy of the reported wave propagation time in commercial acoustic hardware is questionable because of internal filtering. We observed error by

up to 20% by comparing the expected arrival time with the measured arrival time of common metals such as aluminum, stainless steel and nickel. To decouple these internal filtering effects, a separate wave pulser (Compact Pulser) was coupled with an oscilloscope (Picoscope) in order to obtain the raw signal. This new setup was then tested on a cell placed in a pressure holder within an industrial grade temperature-controlled chamber. While the environmental conditions within the TXM chamber cannot be changed, acoustic signals are sensitive to slight fluctuations in the applied pressure and the environmental temperature (e.g. ~100 ns shift for 1°C shift in temperature). Pressure will affect thickness because of separator compressibility. Temperature will change the material moduli. Therefore, these must be tightly controlled to ensure that they do not affect measurement of the wave arrival time. Lastly, spacers were used in between the pouch cell and the transducers, in order to bypass near-field effects and improve signal-to-noise ratio. At distances close to the transducer, wave reflections can cause signal noise and reduce data quality. Rexolite (cross-linked polystyrene) is a common spacer material due to its known low acoustic attenuation and was used in this study.

A number of analyses can determine when a wave "arrives." The main parameter in previous studies was the time-of-flight shift[10]. The time-of-flight shift is calculated using a cross-correlation function that matches different waveform shapes. Each subsequent waveform is compared with an initial reference waveform in order to determine the level of correlation and how much the wave has shifted. The shift in the time-of-flight provides a relative estimate for the longitudinal shift of the entire waveform. However, in the development of a metric for determining the intrinsic mechanical properties, a more accurate determination of the actual wave arrival must be used. In prior acoustic theory in geophysics and other fields, acoustic signal processing typically involves the calculation of the initial wave arrival separate from the surrounding noise, otherwise called the "first break" (t_{first})[21]. The most common method for determining the first break is a windowed average method called short-term-averaging over long-term-averaging (STA/LTA)[21]. The STA/LTA method improves signal-to-noise ratio and allows for more accurate first break picking. The first break represents the transmitted waves with minimum reflections, or the maximum wave propagation speed through the medium, and can hence be used to calculate the wave velocity and effective stiffness.

Figure 2a depicts a sample acoustic signal for the 210 mAh pouch cell that was placed in the pressure holder setup and validated to be accurate after calibration. The first break (t_{first}) in Figure 2c is measured at 75% of the maximum STA/LTA ratio (Figure 2b) of the raw waveform signal (Figure 2a). As depicted, this value fluctuates by no more than 3 ns over time (between 3.320 and 3.323 μs), with the individual shifts being less than 1 ns. The nanosecond resolution is a significant improvement over the commercial pulser/receiver, which samples less frequently and can deviate by over 20 ns (Figure S8). The commercial pulser/receiver is also limited in resolution because the signal contains 495 data points regardless of the range in which it is measured. An acoustic wave measured between 0 μs and 10 μs will contain 495 points, as will a wave measured between 0 μs and 5 μs. The wave arrival should be consistent amongst different transducers and pulser/receivers after zeroing, calibration, and accurate signal processing.
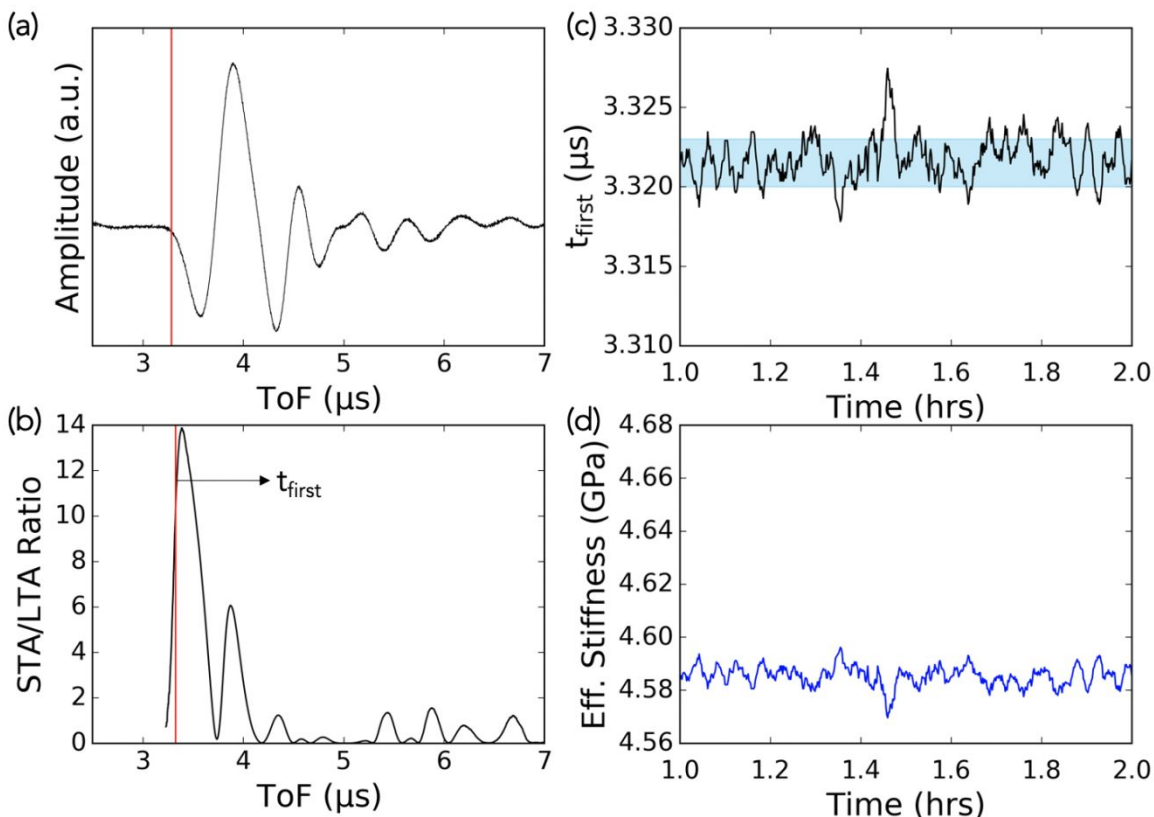
7

Figure 2. Acoustic measurements of the 210 mAh pouch cell from the decoupled pulser/receiver measured at 30°C and 1.4 psi. (a) Sample acoustic waveform. (b) A moving average (short-term average over long-term average, or STA/LTA ratio) is used to determine t_{first}, with the threshold being 75% of the maximum peak. (c) t_{first} (the first break) fluctuates by no more than a few nanoseconds (between 3.320 μs and 3.323 μs) with the decoupled pulser/receiver. (d) The effective stiffness (GPa) is calculated from the first break, cell thickness, and cell density.

3.3. Theoretical consideration of effective stiffness

We briefly describe the theoretical derivation of the effective stiffness from fundamental acoustic wave equations, adapted from Kinsler et al.[22] While earlier studies of acoustic characterization of batteries emphasized the correlation of the acoustic signal with battery charge and health, it is just as important to justify and explain the physical origins from fundamental acoustic equations. A clearer understanding of these relationships allows for quantifiable measurements of mechanical properties such as stiffness and sound speed. First, the general wave continuity equation (Equation 1) describes the velocity and density of the medium as the wave propagates through, causing local compressions and expansions.[23] The fractional change in the density is described by the variable 's' in Equation 2, or the 'condensation.' This expression is used to linearize the wave continuity equation (Equation 3).

$$\frac{\partial \rho}{\partial t} + \nabla \cdot (\rho \vec{v}) = 0 \qquad\qquad (1)$$

$$s = \frac{\rho - \rho_0}{\rho_0} \Longrightarrow (s+1)\rho_0 = \rho \tag{2}$$

$$\rho_0 \frac{\partial s}{\partial t} + \nabla \cdot (\rho_0 \vec{v}) = 0 \Longrightarrow \frac{\partial s}{\partial t} + \nabla \cdot \vec{v} = 0 \tag{3}$$

Second, Euler's force equation describes the net force acting upon the medium (Equations 4-5). An incremental element is arbitrarily chosen to describe the differential force acting locally, which is equated with Newton's second law (Equations 6-7). The second acceleration term is assumed to be negligible in the total derivative of acceleration. Solving this equality, a linearized Euler's equation is obtained, describing the differential pressure acting locally. These linearized equations (Equations 3 and 7) are combined by taking the divergence of the linearized Euler's equation (Equation 8) and the time derivative of the linearized wave continuity equation (Equation 9).

$$P = \frac{f}{A} \Longrightarrow f = P * A \tag{4}$$

$$d\vec{f} = \left[P - \left(P + \frac{\partial P}{\partial x} dx \right) \right] dA = -\nabla P \, dV \tag{5}$$

$$d\vec{f} = \vec{a} * dm \text{ where } \vec{a} = \frac{d\vec{v}}{dt} = \frac{\partial \vec{v}}{\partial t} + (\vec{v} \cdot \nabla)\vec{v}, \text{ and } dm = \rho_0 dV \tag{6}$$

$$-\nabla P \, dV = \rho_0 \, dV * \left(\frac{\partial \vec{v}}{\partial t} + (\vec{v} \cdot \nabla)\vec{v} \right) \Longrightarrow -\nabla P = \rho_0 \left(\frac{\partial \vec{v}}{\partial t} \right) \tag{7}$$

$$-\nabla^2 P = \nabla \rho_0 \left(\frac{\partial \vec{v}}{\partial t} \right) \tag{8}$$

The difference between the two equations results in the second order partial differential equation (Equation 10), which can be further expressed in terms of pressure and density using the definition of condensation (fractional pressure change). As high frequency ultrasonic wave fluctuations are relatively small, only the first term in a Taylor expansion of pressure needs to be considered (Equation 11), which results in a simple relationship between pressure, condensation, and an effective stiffness term. As shown by Equation 11, this derivation of the effective stiffness from acoustic wave physics shows that it is a uniform volume compression term acting in three dimensions. Again, we refer the interested reader to Kinsler et al. for a complete derivation.[22] Fluid/solid composites such as the electrolyte-wetted electrodes in a pouch cell will differ in a non-linear fashion from the pure solid or pure fluid components. However, the measured quantity from acoustics should describe the properties of the bulk material, regardless of whether it can be linearly decoupled into fluid and solid components. This acoustically derived effective stiffness is contrasted with Young's modulus, which is a constant of proportionality in one dimension such as a thin rod, commonly used in tensile testing. Due to the complex composite nature of a battery pouch cell, we posit that an effective stiffness from acoustic interrogation would be a more universal parameter for characterizing the overall structure than a one-dimensional Young's modulus or a stress measurement. The effective

stiffness completely specifies the overall stiffness properties of a heterogeneous material and is an intrinsic material property. Therefore, while the stress or stack pressure may change for different cell sizes or geometries, the stiffness should remain the same.

Substitution of Equation 11 into Equation 10 replaces the condensation term with pressure and results in the second order differential equation (Equation 12). This can be rearranged into the classical wave equation, which shows that the coefficient term is proportional to the acoustic wave velocity, and that the effective stiffness term is simply the product of material density and the square of the compressional wave velocity. Given the assumptions made in this derivation, this equation holds for *linear* acoustic waves, or waves that incur negligible changes in local density. For ultrasonic waves of frequency > 1 MHz as used in this case, the local density changes are minimal and can be neglected.

$$\rho_0 \left(\frac{\partial^2 s}{\partial t^2} + \nabla \cdot \frac{\partial \vec{v}}{\partial t} \right) = 0 \tag{9}$$

$$\rho_0 \frac{\partial^2 s}{\partial t^2} = \nabla^2 P \tag{10}$$

$$P = \left(\frac{\partial P}{\partial \rho} \right)_{\rho_0} (\rho - \rho_0) = \rho_0 \left(\frac{\partial P}{\partial \rho} \right)_{\rho_0} * \frac{(\rho - \rho_0)}{\rho_0} = M_{eff} * s \tag{11}$$

$$\frac{\rho_0}{M_{eff}} \frac{\partial^2 P}{\partial t^2} = \nabla^2 P \implies \nabla^2 P = \frac{1}{c^2} \frac{\partial^2 P}{\partial t^2} \text{ where } c^2 = M_{eff}/\rho_0 \tag{12}$$

Based on Equation 12, the effective stiffness can be determined if the wave velocity and the material density are known. The wave velocity can be determined from the first arrival of the wave and cell thickness. To confirm that the measured wave velocity is accurate, calibration metals of known thicknesses and wave velocities were tested. Table 4 indicates metal foil thicknesses above 500 μm in thickness are accurately measured, whereas foil thicknesses less than 250 μm are underestimated. We attribute this error to the greater impact of the acoustic gel couplant at these lower thicknesses. The liquid gel couplant, which is necessary to induce low acoustic attenuation at the interface, is of a finite thickness and should be accounted for. Liquid gel couplant typically has a relatively lower wave velocity of around 1500 m/s (similar to water) and would therefore result in a significant underestimation of the wave velocity for thin metal foils where the couplant contributes to a greater proportion of the total propagation path. Fortunately, pouch cells are 500 μm thick at the minimum and can be accurately measured. To confirm the consistency of results regardless of battery thickness, pouch cells were constructed with n = 1 to n = 30 layers, with one layer (n = 1) being defined as: anode + separator + cathode. The subsequent layer is then: cathode (other side) + separator + anode. n = 30 is the full 210 mAh LiCoO$_2$/graphite pouch cell, with 15 double-sided cathodes and 16 double-sided anodes. A schematic of the configuration is demonstrated in Figure 1. In Figure 3b, the last data point corresponds to n = 34, which was obtained from a slightly thicker commercial pouch cell of the same chemistry and configuration. The resulting thickness vs first break (Figure 3b) shows a linear relationship, indicating a constant wave velocity of approximately 1700 m/s and resulting in a calculated effective stiffness of 4.76 GPa (Figure 3a). Therefore, the measured wave velocity

and the resulting effective stiffness is confirmed to be the same regardless of how many repeating cell layers there are, and thicker cell stacks do not slow down the wave velocity. The measurement of 4.76 GPa is comparable to a prior ex situ study by Knehr and Hodson[12], where a digital caliper was used to measure the pouch cell thickness. The careful calibration and confirmatory studies here demonstrate the reliability of the acoustic measurement not only for relative shifts but also in calculating an intrinsic material stiffness.

	Measured velocity (m/s)	Reference velocity (m/s)	Calculated effective stiffness (GPa)	Reference effective stiffness (GPa)
Aluminum (3.37 mm)	6560	6320 [23]	98	105
Rexolite (6 cm)	2250	2350 [24]	5.32	3.1
Nickel (500 μm)	6250	5631 [21]	348	258
SS316 (254 μm)	2920	5664 [21]	68.2	251
Brass (150 μm)	2143	4394 [21]	40.1	161

Table 4. Calibration metals to confirm accuracy of wave velocity measurements. The measured velocity is calculated from the measured thickness (using a digital caliper) divided by the wave arrival time. The reference velocity is found from literature as cited. Calculated effective stiffness is converted from measured velocity using $M_{eff} = \rho v_p^2$, where $v_p = L/t_{first}$. Reference stiffness is calculated from $K + 4/3\mu$ using literature values for K and μ. Rexolite is a cross-linked polystyrene used as a spacer because of its optimal acoustic properties (low acoustic attenuation). SS316 represents stainless steel 316 alloy. All tests were conducted in the pressure controlled acoustic holder and in a constant temperature chamber, using the decoupled pulser/receiver acoustic setup (see Experimental Methods section). Metal thickness 500 μm and above are accurate (green), while thicknesses 250 μm and less are less accurate (red), presumably due to the finite thickness of the liquid couplant and other surface roughness effects.

3.4. Effect of cell layers on acoustic wave velocity

We have shown that the effective stiffness of a commercial pouch cell battery can be accurately determined from the wave velocity and cell thickness. The wave velocity and cell thickness can be determined in *operando* by the TXM/acoustics setup to track stiffness changes during battery cycling. The calibration metals used show that the effective stiffness is accurate for material thicknesses above 250 μm. However, a pouch cell is different from a bulk metal due to the cell comprising multiple layers. There are two length scales to consider here. One is the composite nature of a graphite anode or $LiCoO_2$ cathode, which consist of the graphite or $LiCoO_2$ with binder/conductive carbon, wetted with electrolyte. The effective stiffness of this material can be estimated with Voigt, Reuss, or Hashin-Shtrikman bounds which take into account the relative volume fraction of the individual materials (graphite particles, binder, conductive carbon), as reported by previous literature.[25] The second length scale to consider is the repeating layers within a pouch cell. For example, the commercial pouch cell used in this study consists of 30 layers, with each layer composed of an anode and cathode with their respective current collectors and separator layer. The moduli of each of these materials layered in repeated units do not necessarily scale linearly. In geophysics, layer stratification is typically quantified via Backus averaging, which is a harmonic average of the modulus of each layer.[26]

The Backus average of the entire pouch cell stack can be measured if the modulus of each of the layered materials is known. There are 16 copper current collector layers with moduli of 117 GPa[28], 15 aluminum current collector layers with moduli of 69 GPa[30], 32 graphite composite layers with moduli of 5.5 GPa (as estimated with Hashin-Shtrikman bounds)[27-28], 30 LiCoO$_2$ composite layers with moduli of 12 GPa (as estimated with Hashin-Shtrikman bounds)[29], 32 separator layers with moduli of 1.5 GPa[31], 2 polymer pouch layers with estimated moduli of 2 GPa, and enclosed with 2 aluminum layers with moduli of 69 GPa. Therefore, there are 129 individual material layers through which the acoustic wave passes through (Table 5). This is excluding the front ceramic plates of the transducers, which have been accounted for in the initial zeroing and calibration.

The determination of metal and polymer material moduli are straightforward and taken from literature values. To verify the estimated moduli of the composite electrodes, they were stacked in various layers and acoustically interrogated. As shown in Figure 3a, the graphite/Cu electrode has a modulus of 10.7 GPa, and the LiCoO$_2$/Al electrode has a modulus of around 27.8 GPa, as calculated from the measured wave velocities (Figure 3c) and the respective weighted densities of the double-sided electrodes. These values are slightly higher than the respective Hashin-Shtrikman bounds because the measured electrodes include the metal current collector which has a higher modulus. The values are lower than the single particle graphite or LiCoO$_2$ because the composite electrodes are weighted down by the softer materials. The change in thickness of these individual electrodes during cycling can also be estimated from average peak-to-peak spacing of the intensity line profiles generated from TXM micrographs (Figure S3). These peak-to-peak intensities vary because of pouch cell manufacturing tolerances: the electrodes are not perfectly aligned within the cell, causing signal blurring at electrode boundaries. This percent error in thickness calculation is minimized by introducing threshold values for peak discrimination. The results of the peak spacing analysis (Figure S4) show that the average single layer expands upon charge and contracts upon discharge, and that the degree of hysteresis grows with current rate. The initial average electrode thickness of 170 μm confirms the ex situ digital caliper measurements of individual electrodes (180 μm for LiCoO$_2$/Al and 200 μm for graphite/Cu) and the moduli estimation of 27.8 GPa for LiCoO$_2$/Al and 10.7 GPa for graphite/Cu. Unfortunately, the differences in thickness changes between LiCoO$_2$/Al and graphite/Cu during cycling are hard to discern due to the imperfect alignment of the electrode layers with the X-ray detector. For future studies, improved spatial resolution at the single electrode length scale would be aided by tests of single-layer pouch cells, where thicknesses of the single anode and cathode could be measured more accurately without stack distortion.

Component	Bulk Modulus (GPa)	Number of Layers
Graphite composite	5.5 [27-28]	32
LiCoO$_2$ composite	12 [29]	30
Copper current collector	117 [28]	16
Aluminum current collector	69 [30]	15

Separator	1.5 [31]	32
Polymer pouch	2 est.	2
Aluminum pouch	69 [30]	2

Table 5. 210 mAh pouch cell properties for Backus average determination of the total effective stiffness.

The Backus harmonic average of the above values in Table 5 provides an estimate of 4.13 GPa, compared with the acoustically measured value of 4.76 GPa. Therefore, the Backus average is an appropriate bound for an effective stiffness estimation of battery pouch cells, as it is for other heterogeneous layered materials such as those found in geophysics.

$$M_{eff,cell} = n * \left(\sum_{i=0}^{n} \frac{1}{M_{eff,i}} \right)^{-1} = \frac{129}{\frac{16}{117} + \frac{15}{69} + \frac{32}{5.5} + \frac{30}{12} + \frac{32}{1.5} + \frac{2}{69} + \frac{2}{2}} = 4.13 \text{ GPa}$$
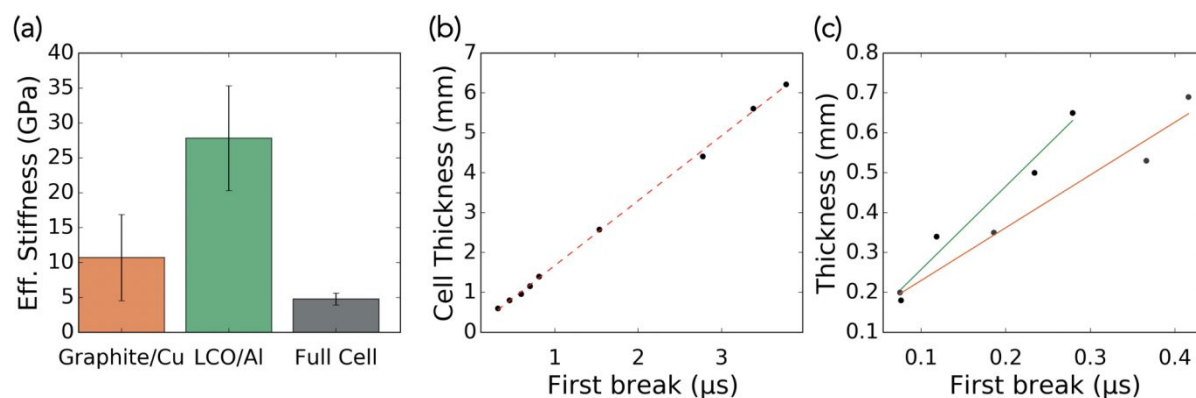

Figure 3. (a) Effective stiffness (GPa) for graphite/Cu electrodes, LiCoO$_2$/Al electrodes and the full pouch cell, as calculated from the wave velocity. (b) Cell thickness (mm) vs first break (μs) of pouch cells with n layers (n = 1 to 5, n = 10, n = 20, n = 30, n = 34); slope indicates wave velocity of ~1720 m/s. (c) Thickness (mm) vs first break (μs) of LiCoO$_2$/Al (green) and graphite/Cu electrodes (orange).

3.5. Correlating cell thickness with effective stiffness in *operando*

The validated wave velocity of 1720 m/s from the slope of Figure 3b can be used to calibrate the *operando* TXM/acoustics results, which are now plotted in Figure 4. As the initial TXM/acoustics setup utilized commercial acoustic hardware which assumes a 4000 m/s wave velocity, the reported values can be scaled with the measured velocity of 1720 m/s. The relationship between measured cell thickness and calibrated wave arrival time reveals an important trend: an increase in the total cell thickness on charge correlates with a faster wave arrival time, and a decrease in the total cell thickness on discharge correlates with a slower wave arrival time. This agrees with prior results indicating that the ~3x higher bulk modulus of lithiated graphite dominates the acoustic time-of-flight (ToF) signal.[12] We recall the distinction between acoustic ToF shift and first break: while the former is a cross-correlation of the full waveform and determines the relative shift, the first break is the time of arrival of the initial wave, which is related to the effective stiffness, explained in Section 3.3. The ToF shift is

calculated from a convolution integral[10], whereas the first break is determined from signal-to-noise processing, widely used in the geophysics field for seismic wave arrival detection.[21]

The cells were cycled according to the protocol listed in Table 3. Figure 4 depicts the typical intracycle trends, showing cycles 2 thru 5 for the three rates examined in this study. The first break (t_{first}) is inversely correlated with the cell thickness and effective stiffness. As the thickness increases on charge, the cell becomes stiffer, and the wave arrives faster. Compared with the 1C rate, the 3C rate underwent sudden mechanical expansion on the initial charge (as shown in Figure 6), and hence the thickness starts at a higher value in Figure 4c. Compared with the shifts on charge and discharge observed in Figure 4a for 1C, the 3C rate experiences a lower magnitude of intracycle shifts, because the cell hits the voltage cutoff earlier and is less fully lithiated. For example, the 1C rate cell is around 4.5 GPa at the start of cycle 3, increases to 5.5 GPa at the end of charge, and decreases back to 4.5 GPa at the end of discharge. The 3C rate cell is around 6 GPa at the start of cycle 3, remains at the same value at the end of charge, and decreases to 5.4 GPa at the end of discharge. Similarly, the approximate single layer thickness changes (Figure S4) indicate stable fluctuations between 170 μm and 175 μm for the 1C rate, an increase to 190 μm for the 2C rate, and nearly 200 μm for the 3C rate.
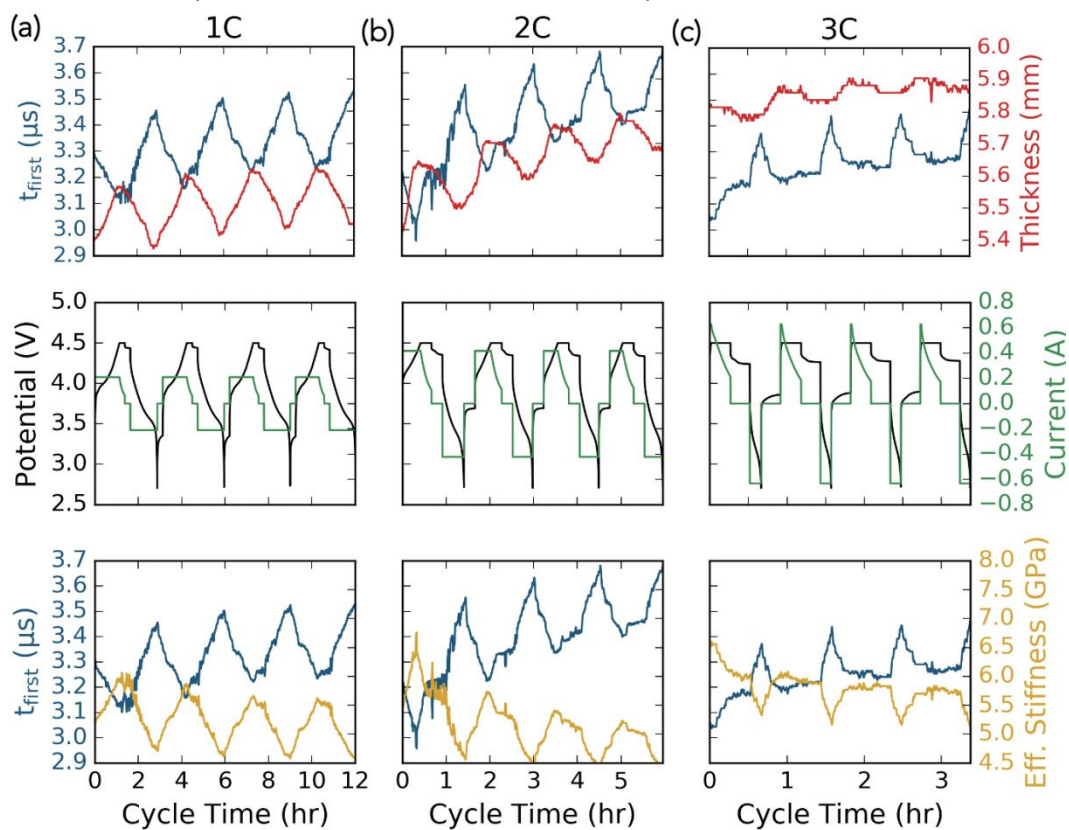

Figure 4. First break (μs), voltage (V vs Li$^+$/Li) and current (A) profile, cell thickness (mm) and effective stiffness (GPa) trends for the first four cycles of three different cells cycled at (a) 1C, (b) 2C, and (c) 3C. All cycling was done using a CCCV charge protocol to 4.5 V and C/30 cutoff and CC discharge protocol to 2.7 V.

Further analysis of state-of-charge dependency is shown in Figure 5, by re-plotting against the total charge passed for each cycle. Again, note that the very first cycle along with every subsequent 5th cycle is not shown but can be observed in Figure 6. Interestingly, the relatively linear correlations on charge and discharge at the 1C rate become non-linear at the higher rates. For the 2C rate, the first arrival reverses direction before the top of charge (Figure 5a); this is in-line with our prior work on detection of Li plating using the ToF shift parameter.[32] While that work utilized relative shifts in the wave arrival, the first arrival measured here along with the inflection point in the thickness (Figure 5b) show that the effective stiffness begins to decrease before the end of charge (Figure 5c). Detailed reports on the acoustic detection of Li metal plating in the same cell chemistry and configuration can be found in Bommier et al.[32]

By taking the capacity losses for each cycle and plotting against the peak-to-peak magnitudes of the stiffness, a linear relationship emerges indicating high correlation coefficients for each of the three rates (Figure 5d). This shows that the intracycle shifts in wave arrival, thickness and stiffness are proportional to the total charge passed. As each cell attains lower states of charge throughout cycling, it also undergoes proportionally less cell expansion and changes in sound speed.
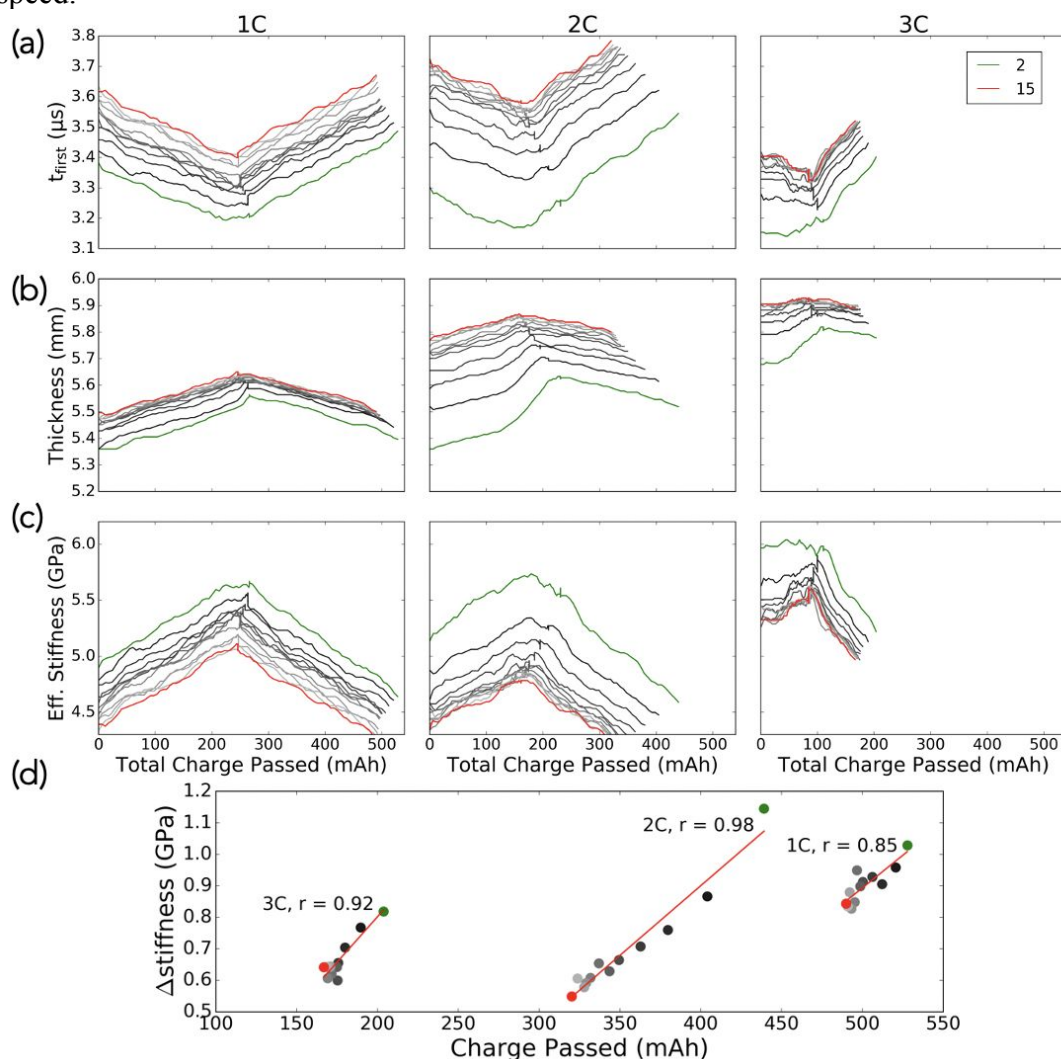
Figure 5. (a) First break (μs), (b) thickness (mm), and (c) effective stiffness (GPa) for the 1C, 2C, and 3C rate cells plotted against the total charge passed for each cycle (charge + discharge capacity, mAh). The green point indicates cycle 2, the red point indicates cycle 15, with cycles in between in order of increasing transparency. (d) Linear regression analysis of the peak-to-peak stiffness changes and the capacity differences for each cycle.

The relationships between the effective stiffness, cell thickness, and first break over the entire duration of cycling is depicted in the plots in Figure 6. The start and end of charge is depicted by the red triangles and red circles, respectively. The start and end of discharge is depicted by the blue triangles and blue circles, respectively. As shown in Figure 6a and mentioned earlier, the 3C cell experienced rapid thickness expansion during the initial charge. The slope of the trends in Figure 6a depicts the sound speed as the pouch cell is cycled. The overall trend in Figure 6b indicates the cell becomes less stiff during cycling. This initial softening of the pouch cell can be compared with a recent study using acoustics to probe cathode wetting dynamics.[12] It was shown by a combination of acoustics and porosimetry that an initial partially wetted cathode in a pouch cell of identical chemistry and configuration was gradually wetted during initial cycling due to stack pressure from expanding graphite anodes. This phenomenon causes a gradual decrease in the effective stiffness over the initial ~12 cycles post-formation, as observed here for all three cycling rates. From the calculated effective stiffness, a rough conversion to applied stack pressure indicates a value of around 300 kPa, which is within the 50 - 500 kPa low stack pressure range described by Cannarella and Arnold using a constant thickness rather than constant pressure cell (see Supplementary Material for calculations and Figures S9-10).[33] Movies of acoustic, tomographic, and effective stiffness evolution over cycling can be found in the Supplementary Materials (Movie M1, M2, M3 in ESI).
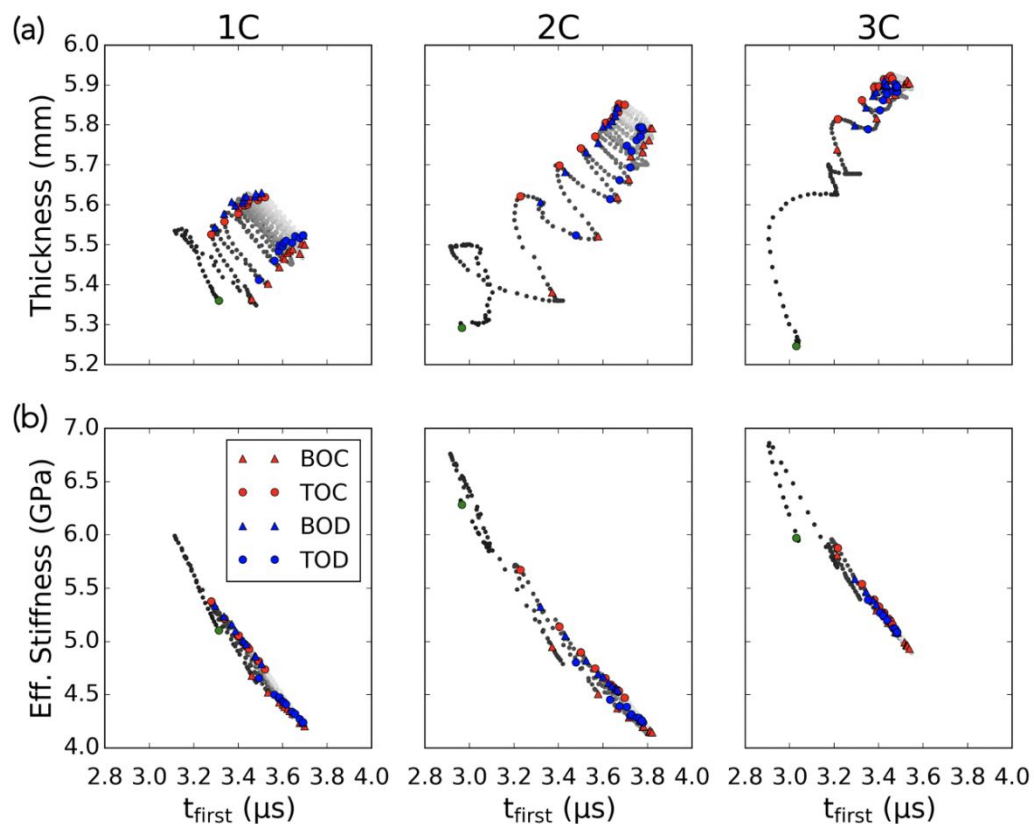
Figure 6. Mechanical expansion dynamics at 1C, 2C, and 3C rates for all cycles, showing cyclical relationship between effective stiffness, cell thickness, and first break. Charging regions are between the red triangle (bottom-of-charge, or BOC) and red circle (top-of-charge, or TOC). Discharging regions are between the blue triangle (bottom-of-discharge, or BOD) and blue circle (top-of-discharge, or TOD). (a) Cell thickness (mm) vs t_{first} (μs). (b) Effective stiffness (GPa) vs t_{first} (μs).

The calculated effective stiffness of 4.76 GPa for the full cell is more similar to that of a soft polymer (~1 GPa) than a hard metal (> 50 GPa). This is because of the abundance of electrolyte wetted separators in the cell as well as the wetting of the graphite and $LiCoO_2$ electrodes. Similarly, the calculated moduli of $LiCoO_2$/Al and graphite/Cu are lower than existing literature values for pure graphite (30 GPa) or $LiCoO_2$ particles (~170 GPa). The wetted graphite or $LiCoO_2$ composite materials have significantly lower moduli than their dry counterparts. The cell and electrode layers can essentially be viewed as a heterogeneous liquid/solid composite.

4. CONCLUSION

By applying rigorous and well defined acoustic elastic theory from other fields to closed form electrochemical energy storage:

1) Acoustic waveforms can be used to estimate the effective stiffness of active storage materials, if calibrated and measured in a tightly controlled environment. We posit that this volume compressional modulus of 4.76 GPa (with an increase of around 1 GPa

during charge and decrease of 1 GPa during discharge) is a more representative measurement than a unidirectional Young's modulus term for a battery cell stack, because it acts in all directions rather than uniaxially. The effective stiffness completely specifies the stiffness properties of the cell regardless of geometry and size and is an important parameter, in addition to stress and strain measurements, for battery chemo-mechanics.

2) Transmission X-ray microscopy was chosen to image cell thickness changes during cycling, though any other simple in-line thickness monitor (e.g. linear displacement sensor) could also be used in lieu of TXM. The initial impetus for using the TXM was to see whether we could observe individual thickness changes of each electrode or lateral heterogeneity in thickness, though these phenomena proved to be more difficult to image.

3) Bulk mechanical characterization is just as important as electrochemical and chemical characterization. Future acoustic applications to commercially relevant pouch cells beyond Li-ion chemistries would unveil even more significant structural changes.

Given the established capabilities of acoustic characterization in other fields, we have shown in this work it can be used to directly measure the intrinsic material state properties within a battery. With accurate measurements of both cell thickness and wave arrival time, the effective stiffness and wave velocity can be reliably determined. We hope that the validation of signal accuracy and repeatability through careful measurements and improved signal processing aid others interested in setting up and using the technique for battery characterization. These new findings may be incorporated into acoustic models for battery characterization and improve prediction accuracy for battery state-of-charge, state-of-health, and state-of-structure.

AUTHOR INFORMATION

Corresponding Authors
*Daniel Steingart (dan.steingart@columbia.edu), Jeung Hun Park (jeungp@princeton.edu)

CRediT Authorship
W.C., D.S. – Conceptualization. W.C. – Investigation, methodology, data curation, writing: original draft, writing: review and editing. R.M. – methodology (acoustic signal processing). A.K. – Investigation (TXM). A.R., G.D., K.D. – helped with acoustic technique. J.H.P. – Supervision. D.S. – Writing: review and editing, supervision, funding acquisition.

Conflicts of Interest
D.S. is a founder of Feasible, which employs the ultrasonic technique (patent application #20160223498) used herein. Feasible did not fund the work nor participate in its execution.

REFERENCES

1   G. T. Kuster and M. N. Toksöz, *Geophysics*, 1974, **39**, 587–606.
2   G. E. Backus, *J. Geophys. Res.*, 1962, **67**, 4427–4440.
3   A. Vary, Acousto-ultrasonic characterization of fiber reinforced composites, *Matls Eval.*, 1982, 40:650.
4   F. C. Beall, *Wood Sci. Technol.*, 2002, **36**, 197–212.
5   D. J. McClements, *Crit. Rev. Food Sci. Nutr.*, 1997, **37**, 1–46.
6   L. R. Taggart, R. E. Baddour, A. Giles, G. J. Czarnota and M. C. Kolios, *Ultrasound Med. Biol.*, 2007, **33**, 389–401.
7   A. G. Hsieh, S. Bhadra, B. J. Hertzberg, P. J. Gjeltema, A. Goy, J. W. Fleischer and D. A. Steingart, *Energy Environ. Sci.*, 2015, **8**, 1569–1577.
8   M. Doyle, T. F. Fuller and J. Newman, *J. Electrochem. Soc.*, 1993, **140**, 1526.
9   J. N. Reimers, J. R. Dahn, *J. Electrochem. Soc.*, 1992, **139**, 2091.
10   G. Davies, K. W. Knehr, B. Van Tassell, T. Hodson, S. Biswas, A. G. Hsieh and D. A. Steingart, *J. Electrochem. Soc.*, 2017, **164**, A2746–A2755.
11   C. Bommier, W. Chang, J. Li, S. Biswas, G. Davies, J. Nanda and D. Steingart, *J. Electrochem. Soc.*, 2020, **167**, 020517.
12   K. W. Knehr, T. Hodson, C. Bommier, G. Davies, A. Kim and D. A. Steingart, *Joule*, 2018, **2**, 1146–1159.
13   J. B. Robinson, M. Pham, M. D. R. Kok, T. M. M. Heenan, J. Dan, L. Brett and P. R. Shearing, *J. Power Sources*, 2019, **444**, 227318.
14   J. B. Robinson, M. Maier, G. Alster, T. Compton, D. J. L. Brett and P. R. Shearing, *Phys. Chem. Chem. Phys.* 2019, **21**, 6354–6361.
15   S. Bhadra, A. G. Hsieh, M. J. Wang, B. J. Hertzberg and D. A. Steingart, *J. Electrochem. Soc.*, 2016, **163**, A1050–A1056.
16   W. Chang, C. Bommier, T. Fair, J. Yeung, S. Patil and D. Steingart, *J. Electrochem. Soc.*, 2020, **167**, 090503.
17   A. Masias, N. Felten, R. Garcia-Mendez, J. Wolfenstine and J. Sakamoto, *J. Mater. Sci.*, 2019, **54**, 2585–2600.
18   E. J. Cheng, N. J. Taylor, J. Wolfenstine and J. Sakamoto, *Journal of Asian Ceramic Societies*, 2017, **5**, 113–117.
19   J. H. Park, A. Raj, A. Kim, G. Davies and D. Steingart, *Microsc. Microanal.*, 2018, **24**, 1910–1911.
20   T. L. Szabo, *Diagnostic Ultrasound Imaging: Inside Out*, Academic Press, 2004.
21   J. H. Kurz, C. U. Grosse and H. W. Reinhardt, *Ultrasonics*, 2005, **43**, 538–546.
22   L. E. Kinsler, A. R. Frey, A. B. Coppens and J. V. Sanders, *Fundamentals of Acoustics, 4th Edition, Wiley-VCH,* 1999, 560.
23   A. E494-10, *Annual Book of ASTM Standards. ASTM International, West Conshohocken, PA*.
24   E. Ginzel, R. Macneil, R. Ginzel, M. Zuber and A. N. Sinclair, *The e-Journal of Nondestructive Testing,* 2015, **20**, 12.
25   X. M. Liu and C. B. Arnold, *J. Electrochem. Soc.*, 2016, **163**, A2501–A2507.
26   T. S and H. Hw, *Appl. Mech. Rev.*, 2002, **55**, B62–B63.
27   K. Persson, Y. Hinuma, Y. S. Meng, A. Van der Ven and G. Ceder, *Phys. Rev. B Condens. Matter*, 2010, **82**, 125416.

28   V. A. Sethuraman, N. Van Winkle, D. P. Abraham, A. F. Bower and P. R. Guduru, *J. Power Sources*, 2012, **206**, 334–342.

29   J. G. Swallow, W. H. Woodford, F. P. McGrogan, N. Ferralis, Y.-M. Chiang and K. J. Van Vliet, *J. Electrochem. Soc.*, 2014, **161**, F3084–F3090.

30   R. B. McLellan and T. Ishikawa, *J. Phys. Chem. Solids*, 1987, **48**, 603–606.

31   M. F. Lagadec, R. Zahn and V. Wood, *J. Electrochem. Soc.*, 2018, **165**, A1829–A1836.

32   C. Bommier, W. Chang, Y. Lu, J. Yeung, G. Davies, R. Mohr, M. Williams and D. Steingart, *Cell Reports Physical Science*, 2020, **1**, 100035.

33   J. Cannarella and C. B. Arnold, *J. Power Sources*, 2014, **245**, 745–751.

TOC Graphic